Repeated lidar acquisitions in an underground salt gallery in the Alsatian potassic basin (France): Monitoring and geomechanical modelling

Guillaume Modeste, Frédéric Masson, Cécile Doubre, François Cornet

Repeated lidar acquisitions in an underground salt gallery in the Alsatian potassic basin (France): monitoring and geomechanical modelling

Guillaume Modeste* (guilem.mod@gmail.com), Frédéric Masson (frederic.masson@unistra.fr), Cécile Doubre (cecile.doubre@unistra.fr), François Cornet

Institut de Physique du Globe de Strasbourg (IPGS), 5 rue René Descartes, 67084 Strasbourg, France

*Corresponding author

Abstract

In the Alsatian potassic basin, located northwest of Mulhouse (eastern France), the deformation of an underground salt gallery is monitored from April 2017 to April 2019 using repeated static lidar acquisitions. This monitoring aims to characterize the rheology of the rock salt. The gallery is situated at 550 m deep in a 20 m thick rock salt layer. At this depth traditional referencing tools such as GPS are not available; and the salt is creeping, which prevents the referencing of the measurements with respect to a stable area. First, we develop a specific acquisition protocol to precisely monitor the deformation affecting the gallery walls over time. After two years, we measure a horizontal deformation between 0.10 and 0.30% all along the gallery with a mean uncertainty of 0.08%. From the low horizontal deformation, a new methodology is developed to set the point clouds in the same coordinate system. By doing so, the gallery closure, or volumetric deformation, is calculated. Then, the horizontal deformation time series of the gallery is used to parametrize the mechanical behaviour law of the rock salt, consistent with parameters from laboratory work on this rock salt. Through our work, in addition to the new methodology, the lidar device is shown to be a useful and polyvalent tool to monitor underground cavities and to mechanically characterize the surrounding medium.

Keywords: Lidar, rock salt, underground cavity, geomechanical modelling, methodology

1. Introduction

Underground galleries might undergo severe deformation induced by the ambient stress state, especially for deep excavations in materials susceptible to creep. Thus, the measurement of the deformation of those galleries is necessary to monitor their stability through time. It also allows improved determination of the rheology of the surrounding medium. Traditional tools, such as an extensometer or a sliding ruler, offer precise values of deformation. However, those values only concern specific points. Unlike traditional tools, *LIght Detection And Ranging* (lidar) devices offer the possibility to measure the distance between a large number of points, allowing the determination of the deformation over a larger spatial extent. During an acquisition or scan, a lidar device derives a volume depiction using laser technology. By measuring the distance from the sensor to many targets, the acquisition collects a set of data forming a point cloud in 3D, representing the scanned volume. Lidar devices have become essential tools for remote sensing and 3D modelling studies, and their fields of application have widened considerably over the last two decades (Eitel et al., 2016; Telling et al., 2017; Wang et al., 2014).

The use of lidar acquisitions to monitor underground galleries is justified by the millimetric accuracy of the measurements (Lichti and Licht, 2006). For superficial excavations such as open-pit mines geo-referencing tools such as GPS are available (Grenon et al., 2017), although not for deep galleries. When the device cannot be set up in the galleries to achieve continuous acquisitions (Cecchetti et al., 2017), the referencing of the acquisitions becomes crucial. In some cases, reflective or optical targets are installed as reference points in a stable area (Kukutsch et al., 2015; Pejić, 2013). In other cases, the point clouds are set in a same coordinate system with a processing based either on cross-correlation methods (Han et al., 2013) or on the Iterative Closest Point (ICP) method (Errington et al., 2010). Moreover, methods based on point clouds cross-correlation result in high accuracy (Lynch et al., 2017). In particular cases, despite the depth, the position of the lidar for the acquisition can be geo-referenced with precision (Delaloye et al., 2015). However, these methods

might be time consuming due to the point cloud processing or to the protocol of acquisition. In order to limit the time spent on these geo-referencing issues, 'global fitting approach' methods have been developed. These methods are based on the comparison of 2D or 3D shapes coming from two point clouds representing the same area (Walton et al., 2018).

The "Mines Domaniales de Potasse d'Alsace" (MDPA) extracted potash from 1910 to 2002 northwest of Mulhouse (eastern France). Due to the depletion of the resource, an underground waste storage site was then created in 1998 to maintain economic activity in the region. The site is located at 550 m deep, in a 20 m thick rock salt layer. Several galleries have been dug both in and around the site to allow the transport and the storage of waste materials. The activity ceased in 2002 due to a fire. The site is currently under observation and is the subject of many studies. Since its creation, the deformation of the site's gallery has been regularly monitored using sliding rulers. This monitoring indicates that the galleries of the waste storage site are slowly closing as a result of rock salt creeping.

Reconnaissance visits have determined that the surface of the rock salt galleries was delaminating. This is explained by the halokinesis. Inside the rock salt layer, salt crystals develop within the natural cracks of the layer. In some cases these new crystals press against the crystals on the surface of the gallery, causing their fall. Thus, we have opposing phenomena: the creeping of the rock salt (decreasing the distance between opposite walls) and the delamination of the superficial salt (increasing the distance). As a consequence, we have chosen to work with specific reflectors, about 70, in order to isolate and measure only the rock salt creeping.

Due to both the creeping and the delamination, we have chosen to avoid the use of cloud point processing in our study such as ICP method (Errington et al., 2010) or 'global fitting approach' methods (Walton et al., 2018). The first phenomenon modifies the position of the points in respect to each other and the second in respect to the roughness of the surfaces. The creeping of the rock salt however prevents the determination and the use of a reference area. Rock salt creeping therefore makes it difficult to implement a common coordinate system for all acquisitions over time.

In this study, we analyse the deformation of an underground salt gallery from April 2017 to April 2019 connected to the waste storage site. This gallery has been monitored by regular static lidar acquisitions, every two to three months. From these repeated lidar acquisitions, precise time series of horizontal deformation or convergence are obtained. Those results are also compared to measurements realized in the neighbouring waste storage site, attesting to the quality of the results. Due to the small amplitude of the deformation after two years, a new methodology has been developed to set the point clouds in the same coordinate system. Thus, the gallery closure, or volumetric deformation, is computed. These time series are then used to parametrize the mechanical behaviour law of the rock salt with a geomechanical model. Through this study, in addition to the new methodology, a lidar device is shown to be a useful and polyvalent tool to monitor underground cavities and mechanically characterize the surrounding medium.

2. Data acquisition

The monitored gallery, oriented N008°W, is 100 m long, 4 m wide, and 2.2 to 3 m high. In order to enable the determination of the deformation, reflective targets are installed every 10 m along the gallery (Figure 1.a). These targets are 2.5 cm radius disks glued to aluminium cubes, which are themselves fixed with a thick vice to the walls and the roof (Figure 1.b-d). For each wall and roof, three cubes are fixed at one-quarter, at half, and at three-quarters of the length and the height (Figure 1.e). Unfortunately, the cubes could not be fixed to the floor, making the monitoring of the vertical deformation more complex.

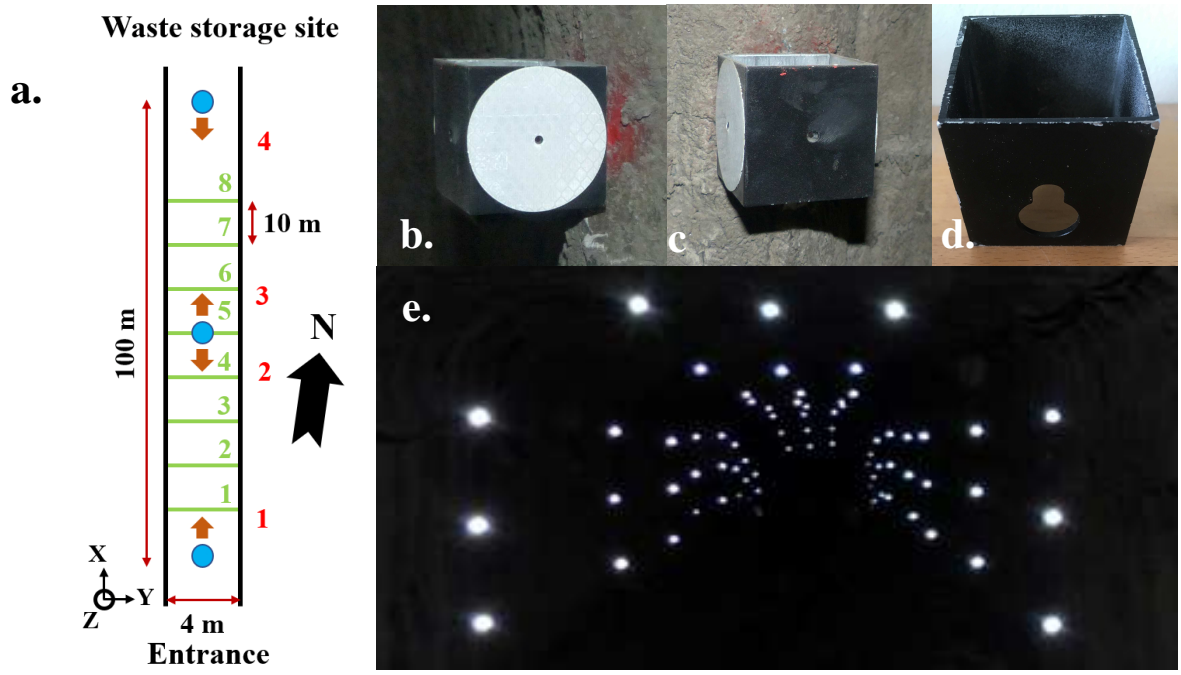

Figure 1 (color) - Schematic drawing of the gallery (a) and pictures of both the reflectors with their cube (b-d) and the gallery (e) (Modeste, 2020)**.** Blue points indicate the three positions of acquisition and brown arrows the direction of the scan. The acquisition numbers are in red. The reflectors are set up in arcs, each arc containing 9 of them and being numbered in green from 1 (entrance of the gallery) to 8 (waste storage site).

From April 2017 to April 2019, ten campaigns of static lidar acquisitions have been conducted, every two to three months. Only one campaign was not undertaken, in August 2018, due to the unavailability of the instrument. The lidar device used is a Riegl VZ-2000 (Petrie and Toth, 2018). This device can scan targets that are at least 2.5 m apart. Each campaign consisted of four acquisitions: one at each end and two at the centre, one in both directions (Figure 1.a). A 360° acquisition at the centre of the gallery was not possible, since the walls were too close to the device.

No area could be considered as stable due to the salt creeping, preventing the presence of a reference point reliable for each acquisition. Therefore, at each acquisition campaign, the lidar was placed vertically below a hook set up on the roof at the beginning of our experiments. The distance between the lidar and the roof is constant over time for each acquisition time. Thus, the lidar is not at the exact same position every time, but at a similar position.

3. Methodology

As indicated in the previous section, the point clouds of each acquisition are not in the same coordinate system at each campaign. In order to monitor the gallery elsewhere than at the location of the reflectors, it is necessary to set the point clouds in the same coordinate system. We have developed a new method for this, which requires two assumptions: point clouds acquired from a similar point and small displacement of the reflectors between the two acquisition times.

In this section, the acquisition realized at the time t_i is associated with the coordinate system i. To transform the coordinates of a point M from the coordinate system i into j, we use the Equation 1:

$$\begin{pmatrix} x_i \\ y_i \\ z_i \\ 1 \end{pmatrix} = s \times \begin{pmatrix} R_{\theta\theta} & R_{\theta\varphi} & R_{\theta\omega} & \frac{T_x}{s} \\ R_{\varphi\theta} & R_{\varphi\varphi} & R_{\varphi\omega} & \frac{T_y}{s} \\ R_{\omega\theta} & R_{\omega\varphi} & R_{\omega\omega} & \frac{T_z}{s} \\ 0 & 0 & 0 & 1 \end{pmatrix} \times \begin{pmatrix} x_j \\ y_j \\ z_j \\ 1 \end{pmatrix} \quad (1)$$

with (x_j, y_j, z_j) the coordinates of the point M in the coordinate system j, (x_i, y_i, z_i) the coordinates of the point M in the coordinate system i, s a scaling factor, (T_x, T_y, T_z) the components of the vector translation, R_{ij} the component of the rotation matrix, θ the angle of rotation around the x-axis, φ the angle around the y-axis and ω the angle around the z-axis.

Assuming similar orthonormal coordinate systems, s is equal to 1. This is consistent with test measurements giving a value of 1.0003 ± 0.0010 (Habib, 2018). The translation and the rotation are geometrical transformations which preserve the distance between two points. Thus, the distance measured during an acquisition campaign is comparable to a distance from another acquisition campaign.

The distance between two points can be written:

$$(AB)_j = \sqrt{\left(x_{bj} - x_{aj}\right)^2 + \left(y_{bj} - y_{aj}\right)^2 + \left(z_{bj} - z_{aj}\right)^2} \quad (2)$$

with $(AB)_j$ the distance between the points A and B at the time t_j, (x_{aj}, y_{aj}, z_{aj}) the coordinates of the point A in the coordinate system j at the time t_j and (x_{bj}, y_{bj}, z_{bj}) the coordinates of the point B in the

coordinate system j at the time t_j. Using the law of conservation of the distances between two points, Equation 2 can be written with the coordinates of the coordinate system i and the displacement vectors (displacements of the reflectors between the acquisition times t_i and t_j):

$$(AB)_j = \sqrt{\left(x_{bi} - x_{ai} + dx_{bij} - dx_{aij}\right)^2 + \left(y_{bi} - y_{ai} + dy_{bij} - dy_{aij}\right)^2 + \left(z_{bi} - z_{ai} + dz_{bij} - dz_{aij}\right)^2} \quad (3)$$

with dx_{aij} and dx_{bij} the displacement along the x-axis of the points A and B between the times t_i and t_j, dy_{aij} and dy_{bij} the displacement along the y-axis of the points A and B between the times t_i and t_j, dz_{aij} and dz_{bij} the displacement along the z-axis of the point A and B between the times t_i and t_j. Here, the vector displacement is expressed in the coordinate system i. In the case of low deformation, with variation of distance of a few millimetres, the displacement difference is small compared to the coordinate difference. Thus, we can assume that the square of the displacement difference can be neglected (Equation 4, 5 and 6):

$$\left(dx_{bij} - dx_{aij}\right)^2 \sim 0 \quad (4)$$

$$\left(dy_{bij} - dy_{aij}\right)^2 \sim 0 \quad (5)$$

$$\left(dz_{bij} - dz_{aij}\right)^2 \sim 0 \quad (6)$$

By using and developing Equations 3 to 6, we have:

$$\begin{aligned}(AB)_j^2 = {} & (x_{bi} - x_{ai})^2 + 2(x_{bi} - x_{ai})\left(dx_{bij} - dx_{aij}\right) + \left(dx_{bij} - dx_{aij}\right)^2 + (y_{bi} - y_{ai})^2 \\ & + 2(y_{bi} - y_{ai})\left(dy_{bij} - dy_{aij}\right) + \left(dy_{bij} - dy_{aij}\right)^2 + (z_{bi} - z_{ai})^2 \\ & + 2(z_{bi} - z_{ai})\left(dz_{bij} - dz_{aij}\right) + \left(dz_{bij} - dz_{aij}\right)^2\end{aligned}$$

$$\begin{aligned}\Leftrightarrow \frac{1}{2}\left[(AB)_j^2 - (AB)_i^2\right] = {} & (x_{bi} - x_{ai})\left(dx_{bij} - dx_{aij}\right) + (y_{bi} - y_{ai})\left(dy_{bij} - dy_{aij}\right) \\ & + (z_{bi} - z_{ai})\left(dz_{bij} - dz_{aij}\right) + o\left[\left(dx_{bij} - dx_{aij}\right)^2\right] + o\left[\left(dy_{bij} - dy_{aij}\right)^2\right] \\ & + o\left[\left(dz_{bij} - dz_{aij}\right)^2\right] \quad (7)\end{aligned}$$

Equation 7 can be written with matrix:

$$\left(\frac{1}{2}\left[(AB)_j^2-(AB)_i^2\right]\right)=\begin{pmatrix}-\Delta x_{abi} & -\Delta y_{abi} & -\Delta z_{abi} & \Delta x_{abi} & \Delta y_{abi} & \Delta z_{abi}\end{pmatrix}\times\begin{pmatrix}dx_{aij}\\dy_{aij}\\dz_{aij}\\dx_{bij}\\dy_{bij}\\dz_{bij}\end{pmatrix} \quad (8)$$

with Δx_{abi} the coordinates difference along the x-axis between points A and B in the coordinate system i, Δy_{abi} the coordinates difference along the y-axis between points A and B in the coordinate system i, Δz_{abi} the coordinates difference along the z-axis between points A and B in the coordinate system i. This is repeated for each combination of reflectors and the matrix is concatenated. Thus, from Equation 8 and for M points, we have:

$$\begin{pmatrix}\frac{1}{2}\left[(AB)_j^2-(AB)_i^2\right]\\\vdots\\\frac{1}{2}\left[(LM)_j^2-(LM)_i^2\right]\end{pmatrix}=\begin{pmatrix}-\Delta x_{abi} & -\Delta y_{abi} & -\Delta z_{abi} & \cdots & 0 & 0 & 0\\\vdots & \vdots & \vdots & \ddots & \vdots & \vdots & \vdots\\0 & 0 & 0 & \cdots & \Delta x_{lmi} & \Delta y_{lmi} & \Delta z_{lmi}\end{pmatrix}\times\begin{pmatrix}dx_{aij}\\dy_{aij}\\dz_{aij}\\\vdots\\dx_{mij}\\dy_{mij}\\dz_{mij}\end{pmatrix} \quad (9)$$

Equation 9 has the form: D = GM, with D the data, G the transfer matrix and M the model. In our case, M is the reflector displacements to be estimated. We can use Equation 10 to solve Equation 9 (Tarantola, 2005):

$$M = M_0 + (G^T C_D^{-1} G + C_M^{-1}) G^T C_D^{-1} (D + G M_0) \quad (10)$$

with M_0 the a priori model, C_D the covariance matrix of the data and C_M the covariance matrix of the model. By solving Equation 10, we obtain the reflectors displacement between the two acquisitions in the coordinate system of our choice. The estimated displacement vectors are in the coordinate system i in the previous equation sequence.

This method requires the use of at least seven distinct reflectors. These reflectors might be placed either within the same arc or all along the gallery. For each reflector, we have three unknowns, the three associated components of the displacement vector. We need at least the same number of unknowns and distances to have a well-defined system. Thus, with seven reflectors, we have 21 unknowns for 21 distances.

By applying the displacement to the reflectors at the time t_i, we obtain the position of the reflectors at the time t_j in the coordinate system i. Thus, at the time t_j, we have the position of the reflectors in both coordinate systems i and j. By concatenating Equation 1 for each reflector, we get Equation 11:

$$\begin{pmatrix} x_{ai} & \dots & x_{mi} \\ y_{ai} & \dots & y_{mi} \\ z_{ai} & \dots & z_{mi} \\ 1 & \dots & 1 \end{pmatrix} = \begin{pmatrix} R_{\theta\theta} & R_{\theta\varphi} & R_{\theta\omega} & T_x \\ R_{\varphi\theta} & R_{\varphi\varphi} & R_{\varphi\omega} & T_y \\ R_{\omega\theta} & R_{\omega\varphi} & R_{\omega\omega} & T_z \\ 0 & 0 & 0 & 1 \end{pmatrix} \times \begin{pmatrix} x_{aj} & \dots & x_{mj} \\ y_{aj} & \dots & y_{mj} \\ z_{aj} & \dots & z_{mj} \\ 1 & \dots & 1 \end{pmatrix} \quad (11)$$

By solving Equation 11 with a least-square method, the transfer matrix between the two coordinate systems can be estimated and then used to set the point clouds in the same coordinate system.

Thus, in this method the point clouds are set into the same coordinate system from reference points whose position has been corrected for the displacement occurring between the two acquisition times. Thus far such a correction was not envisaged to set the point clouds in the same coordinate system. This method is less time consuming than methods based on point clouds cross-correlation since we do not need to work with the whole point clouds (Lynch et al, 2017). However, our method requires installing reflectors to recognize and locate specific points completely during each acquisition, in contrast to 'global fitting approach' methods (Walton et al., 2018).

4. Results

This section is divided into two main parts. First, the uncertainty of distances between reflectors and of deformations is determined. Second, the horizontal deformation time series are analysed. Due to the small amplitude of the deformation, we can set the point clouds in the same coordinate system. Lastly, the closure of the gallery is calculated using the open source software CloudCompare (Girardeau-Montaut, 2011).

a. Uncertainty of distances between reflectors and of deformations

The scan acquisition 1 is repeated twice during the first campaign of acquisitions (case 1, Table 1). Between the two acquisitions, the lidar device is uninstalled and then reinstalled. Each

installation followed the described protocol. The aim is to compare the distances between reflectors inside both collected point clouds. The coordinates of the center of each reflector are extracted from the first point cloud. The distance between each reflector is then calculated from these coordinates. This is repeated for the second point cloud. Lastly, both distance sets are compared; i.e., each distance between reflectors obtained in the first point cloud is compared to its equivalent in the second point cloud.

In this study, the uncertainty is defined as the difference between two distance sets coming from two different point clouds acquired the same day. Thus, the uncertainty reflects the error related to the acquisition of the point cloud and the extraction of the reflector coordinates. The uncertainty is chosen to be greater than 90-92% of the absolute differences between both distance sets. The uncertainty is low, about 3 mm (Table 1). Then we estimate the uncertainty by using only reflectors located within a distance smaller than 40 m of the lidar. This distance corresponds to the maximum distance between each reflecting target and the lidar when it is set up at the centre of the gallery (Figure 1.a). The uncertainty is lower, about 2 mm (Table 1).

In order to assess the importance of the protocol, we realize during the second campaign an additional acquisition 1 without respecting the protocol (case 2, Table 1). The device is shifted by ~50 cm away from the protocol position. This time the uncertainty is 3 times higher, 9 mm with all reflectors and 6 mm with reflectors located at less than 40 m from the lidar (Table 1). This result highlights the importance of respecting the protocol by replacing the device approximately a few centimetres from the original position.

In order to assess the stability of the uncertainty over time, we also repeat the acquisition 1 twice during the tenth campaign in April 2019 (case 3, Table 1). We follow the same procedure for the comparison. The uncertainty is similar to the one obtained for the first campaign (Table 1). Thus, the uncertainty is stable over time and we keep a value of 2.1 mm for the uncertainty on the distance.

Table 1 - Estimation of the uncertainty on the measured distance from lidar acquisitions

	Reflectors	Standard deviation [mm]	Uncertainty [mm]	Rate [%]
Case 1	All	1.7	2.9	90.8
	< 40 m	1.0	2.1	90.8
Case 2	All	4.1	9.1	91.1
	< 40 m	2.6	5.8	90.3
Case 3	All	2.5	2.8	90.5
	< 40 m	3.2	1.9	91.2

In order to estimate the uncertainty on deformations, we use Equation 12, derived from metrology (JCGM, 2008):

$$\Delta\varepsilon(L_i, L_f) = \sqrt{\left(\frac{\partial\varepsilon(L_i, L_f)}{\partial L_i} \times \Delta L_i\right)^2 + \left(\frac{\partial\varepsilon(L_i, L_f)}{\partial L_f} \times \Delta L_f\right)^2} \quad (12)$$

with ε the deformation, L_i and L_f the initial and final distances, Δ refers to the uncertainty. Assuming that the uncertainty on distances is constant over time, Equation 12 can be written as follow:

$$\Delta\varepsilon(L_i, L_f) = \frac{\Delta L}{L_i} \times \sqrt{1 + \frac{L_f^2}{L_i^2}} \quad (13)$$

Taking into account an uncertainty of 2.1 mm on the distances measured with the lidar, the uncertainty on the deformation ranges from 0.05 to 0.10%.

b. Horizontal deformation

After two years, the horizontal deformation develops between 0.10 and 0.30% all along the gallery (Figure 2.a-b). To obtain the amplitudes of the horizontal deformation, we look at the variation of distance between two reflectors on opposite walls, at the same height and inside the same arc. These values are higher than the uncertainty which has a mean value of 0.08%. Thus, the monitored deformation is significant and appears linear over two years. Considering a width of 4 m, the variation of distance between two opposite reflectors ranges from ~4 to 12 mm. Hence, the displacement of each reflector can be considered small.

To assess the quality of the results, we compare ours to available measurements of horizontal deformation in three neighbouring galleries (Figure 2.c). These measurements were carried out by the MDPA with a sliding ruler at reference points marked by nails from June 2007 to June 2013. For the comparison, we use the results from arc 8 (Figure 1.a), which is the arc closest to the waste storage site. In the manual time series (ruler), we note the presence of offsets due to the loss of the initial reference point, the nail falling from the wall. Measurements have been made with a point close to the initial reference point. As shown on Figure 2.c, both measurement types are consistent.

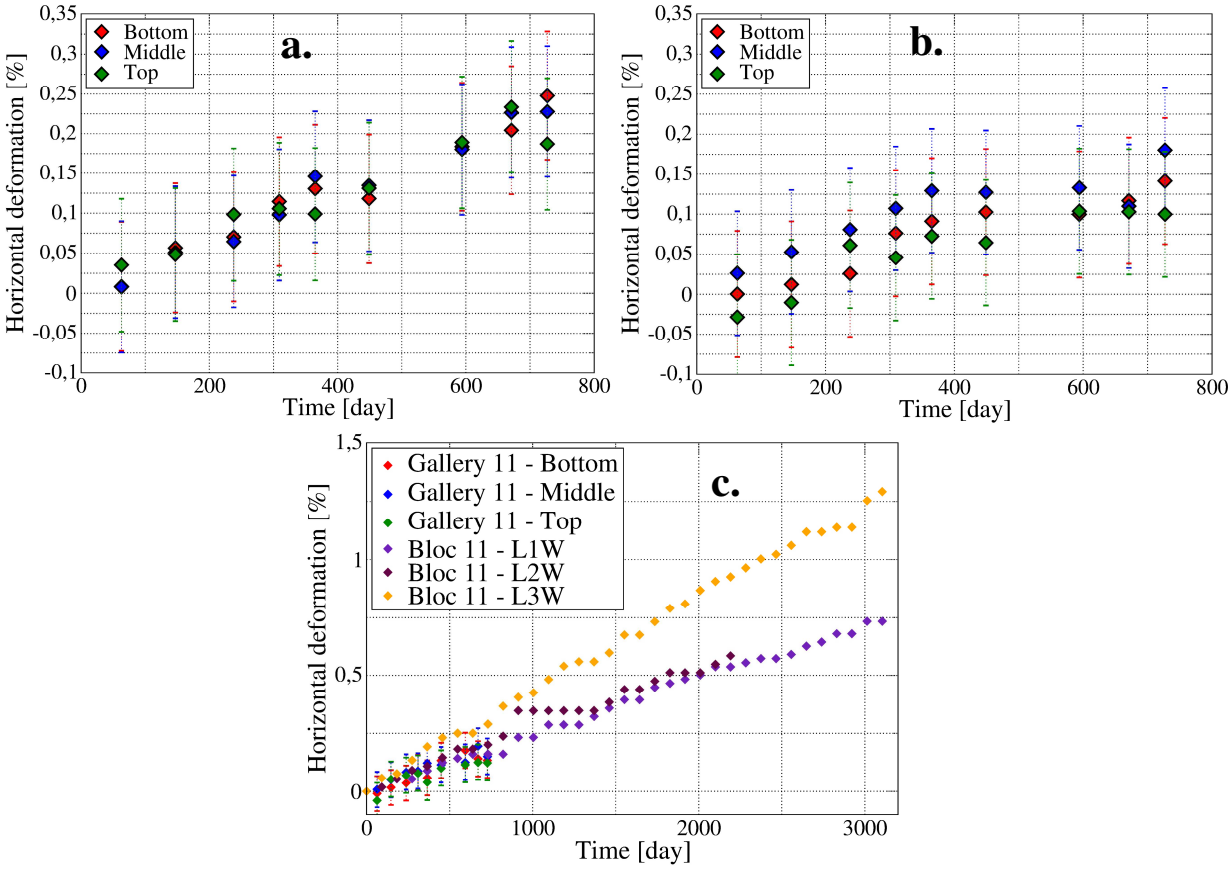

Figure 2 (color) - Horizontal deformation time series from lidar campaigns (a and b) compared to manual available measurements (c) (Modeste, 2020)**.** The plotted measurements correspond to arc 3 (a), 7 (b) and 8 (c). The positive values correspond to a decrease of the distance between the reflectors. 'Top' indicates the pair of reflectors fixed at three-quarters height, 'Middle' at halfway, and 'Bottom'" at one-quarter height. The MDPA data are ruler measurements in three neighbouring galleries, associated with the names "Bloc 11 – LXW". The two distinct reference dates of April 2017

and June 2007 have been chosen for the lidar measurements and for the ruler measurements, respectively.

c. Volumetric deformation

i. Setting point clouds in the same coordinate system with the new method

Since the deformation between the first and the last campaign is low (<0.3%), we can apply our methodology to set our point clouds in the same coordinate system. We do the test with the point clouds coming from acquisitions 2 and 3 (Figure 1.a). The calculation procedure and the different variables are summarised in Figure 3. After inversion, we obtain the displacement vectors of the reflectors from April 2017 to April 2019. The norm of the displacement vectors obtained is of the order of a few millimetres.

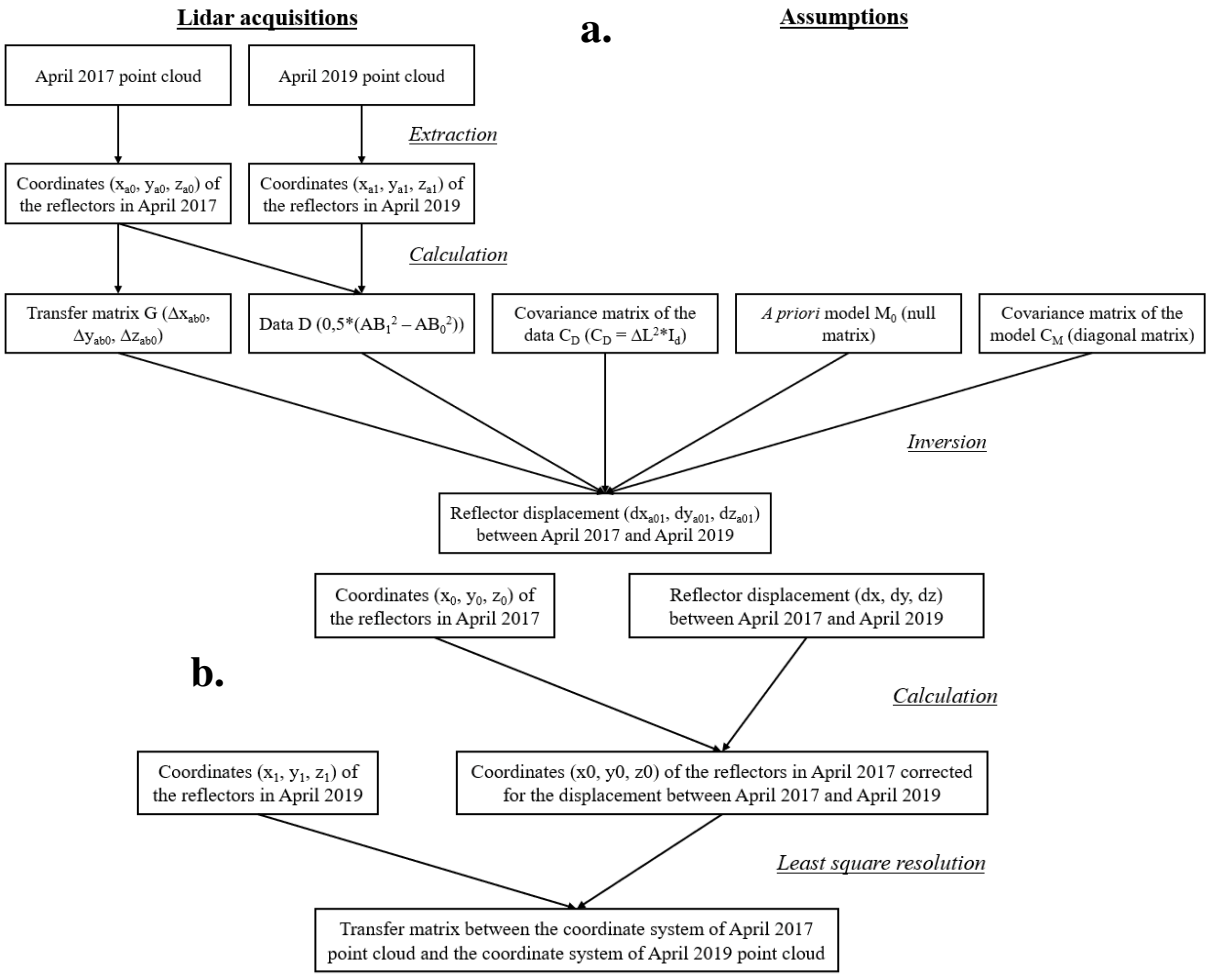

Figure 3 – Flowcharts to compute the reflector displacement between April 2017 and April 2019 (a), and then to deduce the transfer matrix between the two coordinate systems (b)

In order to estimate the quality of the inversion, displacement vectors are applied to the position of their respective reflectors in the point cloud acquired in April 2017. We calculate the distance between each reflector with their new coordinates. Then, we calculate the distance between each reflector in the point cloud acquired in April 2019. Lastly, the two distance sets are compared. The differences between the two distance sets are small, at the order of micrometres (Table 2). Thus, these comparisons validate our methodology. Figure 4 shows reflectors coming from both point clouds before and after being set in the same coordinate system.

Table 2 – Difference of reflectors distance in April 2019 between the original and the adjusted data

Acquisition point	Maximum difference [µm]	Minimum difference [µm]	Standard deviation [µm]

2	48.3	-75.6	10.5
3	95.2	-102	15.9

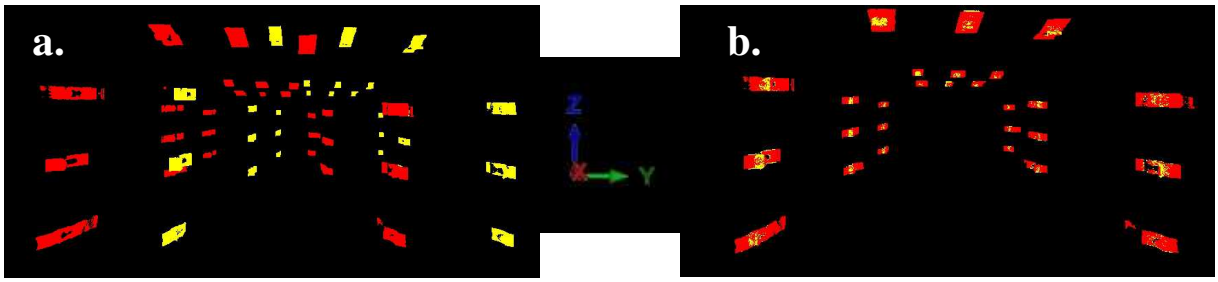

Figure 4 (color) – Reflectors (arcs 1, 2 and 3) from the April 2017 and the April 2019 point clouds before (a) and after (b) having set them in the same coordinate system. The point clouds have been acquired from acquisition point 2. Yellow is associated with the April 2017 point cloud and red with the April 2019 point cloud.

ii. The closure of the gallery

On the open-source software CloudCompare, we study the closure, or volumetric deformation, of four sections of the gallery between the first campaign in April 2017 and the last one in April 2019. To do so, we work only with the point clouds acquired at the centre of the gallery (acquisitions 2 and 3, Figure 1.a). Having the point clouds in a same coordinate system allows us to cut the same section of the gallery at different times. By adding vertical planes on both sides of the selected section, a continuous volume with triangular mesh is created by solving Poisson's equation (Figure 5.a) (Kazhdan et al., 2006). Then, we compute the volume of the retained section. The April 2017 and April 2019 results are finally compared to each other. We repeat this process with three other sections along the gallery (Figure 5.b).

Thus, we obtain four values ranging from 0.34 to 0.55% after two years (Figure 5.b). These values are higher than the horizontal deformation results. As the gallery also deforms vertically (closure), the volumetric deformation is greater than the horizontal deformation. These results are close to the estimations based on the measured displacement of the reflectors. We compare the computed deformation to the variation of the surface of the opening of the gallery, corresponding to

a rectangle. To the initial width of 4 m, we subtract the mean reflector displacement of each opposing wall. To the initial height of 2.5 m, we subtract two times the mean reflector displacement of the roof, since we do not have reflectors on the floor. Then, the product of the initial width and height is compared to the product of the reduced width and height. From this comparison, we estimate the volumetric deformation from the displacements of the reflectors. The estimated values range from 0.44% to 0.52% (Figure 5.b).

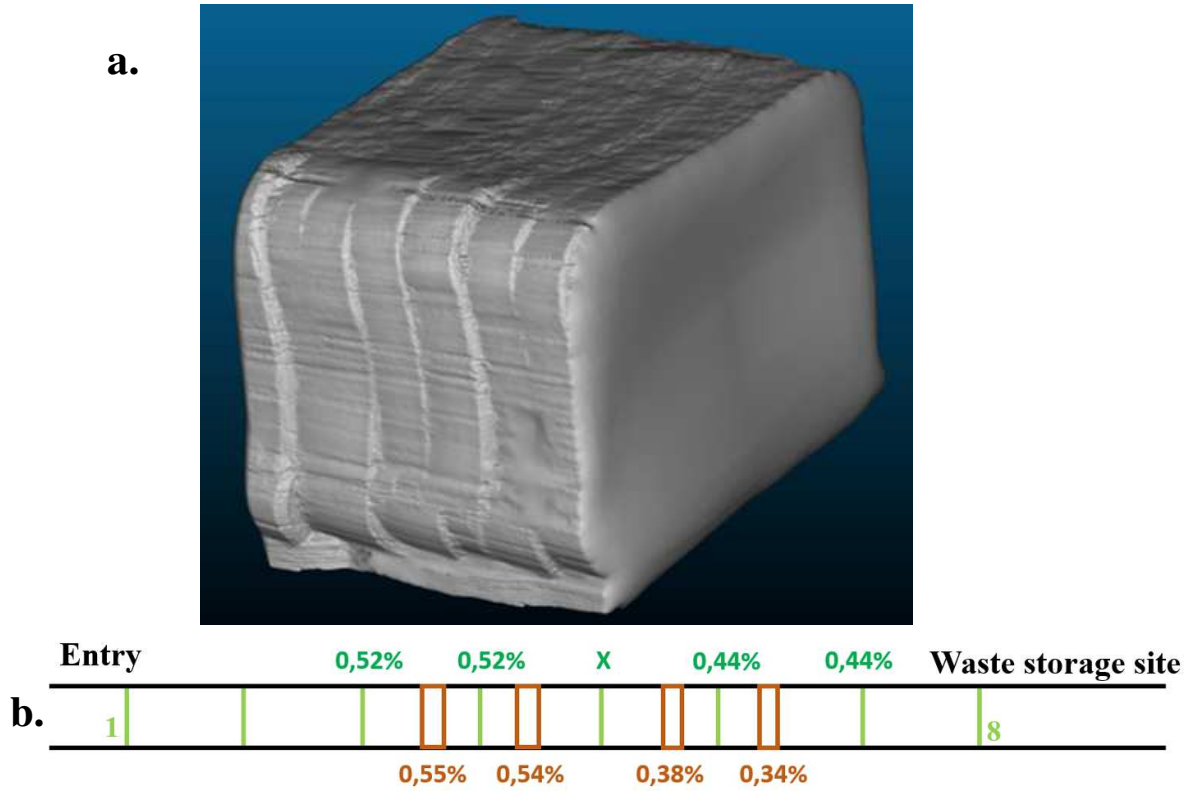

Figure 5 (color) - Created volume from the point cloud (a) and its volumetric deformation after two years (b) (Modeste, 2020)**.** Positive values correspond to a closure or a loss of volume. Numbers in brown are the computed results on CloudCompare while numbers in green refer to the estimation based on the displacement of the reflectors.

5. Geomechanical modelling

In this section, the time series of horizontal deformation are geomechanically modelled. The model is first set up according to the mechanical characteristics of the Alsatian potassic basin. Then,

the deformation of the gallery is modelled to parametrise the mechanical behaviour law of the medium.

1. Model setup

The deformation of two rock salt samples from the Alsatian potassic basin has been studied in the laboratory under different conditions of temperature and deviatoric stress. Ghoreychi (1991) shows that the elasto-visco-plastic behaviour of the rock salt follows Norton's Law (Equation 12, 13, 14):

$$\dot{\varepsilon}_{ij}^{v} = \left(\frac{3}{2}\right)\dot{\varepsilon}_{cr}\left(\frac{\sigma_{ij}^{d}}{\bar{\sigma}}\right) \quad (12)$$

where

$$\dot{\varepsilon}_{cr} = \begin{cases} A\bar{\sigma}^{n} & \bar{\sigma} \geq \sigma_{1}^{ref} \\ 0 & \bar{\sigma} < \sigma_{1}^{ref} \end{cases} (13)$$

and

$$A = \frac{A_s}{\sigma_0^n}\exp\left(-\frac{B}{T}\right) \quad (14)$$

where $\dot{\varepsilon}_{ij}^{v}$ is the creep strain-rate tensor, $\dot{\varepsilon}_{cr}$ the creep rate, σ_{ij}^{d} the deviatoric stress, $\bar{\sigma}$ the Von Mises stress, σ_1^{ref} the Von Mises stress threshold, n the stress exponent, A_s the rate of reference, T the temperature, B the ratio between the activation energy and the universal gas constant, and σ_0 the normalization stress. Norton's law and modified versions are commonly associated with the mechanical behaviour law of rock salts (Khaledi et al., 2016; Wang et al., 2010). For rock salts, the threshold is null, creep occurring as soon as deviatoric stresses are present in the medium (Carter et al., 1993). Empirical parameters are summarised in Table 3. Previous studies (Camusso and Billaux, 2013; Laouafa et al., 2010) focused on the modelling of the horizontal deformation time series coming from the ruler measurements. In these studies, the authors used other values of reference velocity A_s, between 0.015 and 0.022 %/day instead of 0.005%/day, to retrieve the measurements.

Table 3 - Norton's Law parameters

Parameter	Symbol	Value
Power exponent	n	4.0
Reference velocity	A_s	0.005 %/day
Related to the activation energy	B	4700 K
Normalized stress	σ_0	1.0 MPa

In this work, we use Flac3D, which is commercial software developed by Itasca that allows the study of the mechanical behaviour of a continuous three-dimensional medium (Itasca, 2002). This modelling aims to determine which value of the reference velocity A_s in Norton's Law is relevant. To model the gallery, a rectangular parallelepiped at 26.4 m high, 24 m wide and 52 m long is drawn with rectangular parallelepipeds at 0.6 m high and 0.8 m long and wide (Figure 6). With those dimensions, the gallery is made up of five parallelepipeds wide and four in height, either a node at 0.6, 1.2 and 1.8 m of height. These positions are equivalent to those of the reflectors in the gallery. Since the height of the model (26 m) is similar to the thickness of the salt layer (about 20 m), a single layer is modelled. In the modelling, the density, the Young's modulus and the Poisson's ratio used are 2.31 $gm.cm^{-3}$, 28.3 GPa and 0.25, respectively (Table 4). The Young's modulus is different from the laboratory results, 25 GPa (Ghoreychi, 1991), to account for the presence of anhydrite and marls, which have a Young's modulus of 61 and 5.9 to 7 GPa, respectively (Nguyen-Minh and Bergues, 1995; Trippetta et al., 2013). These values and the mechanical behaviour law have been estimated experimentally in laboratory tests on small samples. These results are used here without taking into account potential scale effects.

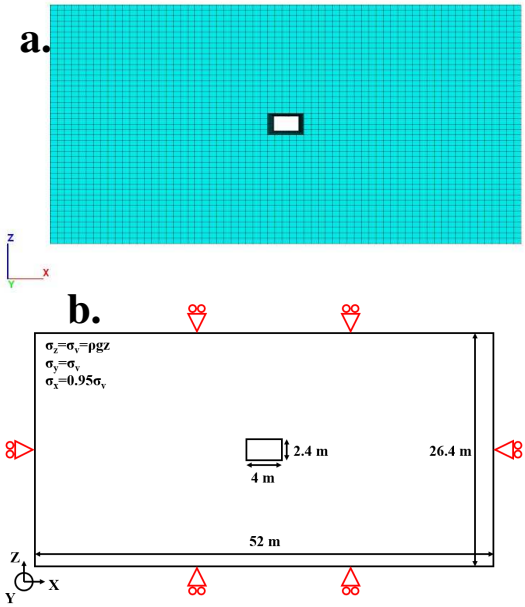

Figure 6 (color) – View of th enter (a) and model scheme (b).

Table 4 – Geomechanical parameter of the geomaterial

Parameter	Symbol	Value
Density	ρ	2.31 g.cm^{-3}
Poisson's ratio	ν	0.25
Young's modulus	E	28.3 GPa

The gallery is nearly oriented along the maximum horizontal stress direction, which is the North-South axis (Baumann and Illies, 1983; Larroque, 1987). According to in-situ stress measurements in the Alsatian potassic basin (Cornet and Burlet, 1992), the vertical stress σ_v is nearly equal to the maximum horizontal stress σ_H and the minimum horizontal stress σ_h is equal to $0.95\sigma_v$.

2. Comparisons with the model

After setting up the stress field, the closure of the gallery is then modelled. The centre of the parallelepiped, along the Y-axis/N-S direction, is excavated to model the gallery. Norton's Law with the experimental and geomechanical parameters (Table 3 and 4) are associated with each element.

In the model, the temperature is set to 298 K, which is the temperature measured during the lidar campaigns. The modelling is carried out with different values of A_s. A twenty-year period is first modelled, which is approximately the time between the excavation of the gallery and the beginning of our lidar measurement campaigns. Then, the modelling is pursued over a two-year period that corresponds to our monitoring period. Over this two-year period the distance evolution between each opposite node of the gallery is extracted from the model. The horizontal deformation is then deduced and compared to our lidar time series (Figure 7). The comparison is done between the pair of reflectors fixed at one-quarter height and the pair of nodes at 0.6 m, the pair of reflectors fixed at half height and the pair of nodes at 1.2 m and so on. Thus, only three pairs of reflectors per arc are selected for the comparison between the model and the data. With seven arcs, a total of 21 comparisons are made. A R^2 determinant, reflecting the similarity of the model to the measurements, is calculated for each comparison (Table 5). We used the point clouds coming from acquisitions 2 and 3 to produce the horizontal deformation time series (Figure 1.a). However, with these acquisitions, it is not possible to get the time series of arc 5, for it is too close to the lidar. A mean value of R^2 is obtained for each modelling carried out with a different value of A_s. The modelling carried out with a value of 0.005 %/day for A_s seems to fit our measurements best (Table 5). Here we retrieve results from laboratory experiments, which is 0.005 %/day.

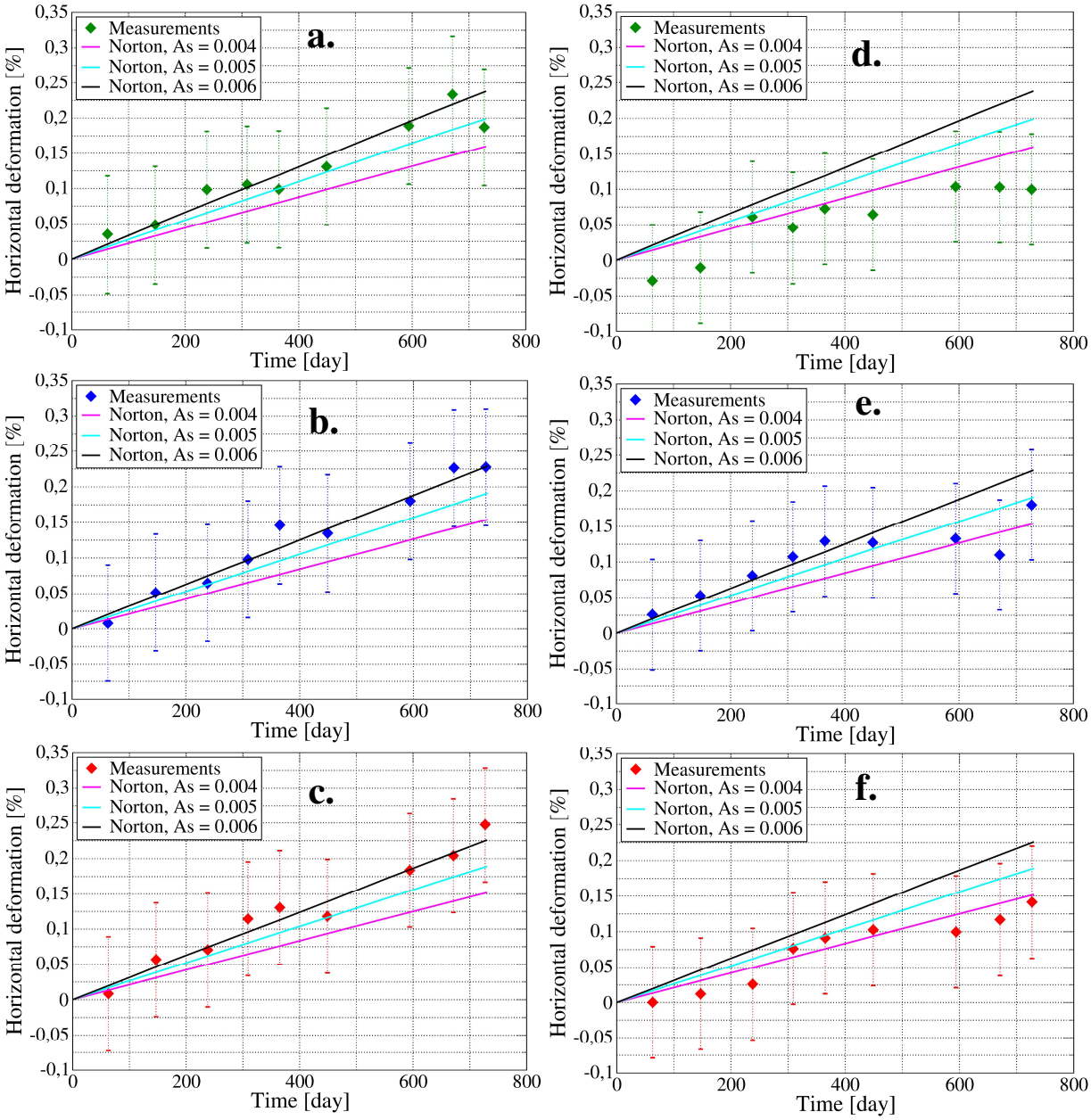

Figure 7 (color) - Comparison between the results from campaigns of lidar acquisition and the geomechanical model (Modeste, 2020)**.** The plotted results correspond to arc 3 (a-c) and arc 7 (d-f). The reflectors are associated with the nodes in the model. The horizontal deformation time series of the pair of reflectors fixed at three-quarters height is compared to the pair of nodes at 1.8 m (a and d), the pair of reflectors fixed at half height to the pair of nodes at 1.2 m (b and e) and the pair of reflectors fixed at one-quarter height to the pair of nodes at 0.6 m (c and f).

Table 5 - R-square determinant of the comparison between the lidar measurements and the model.

	A_s = 0.004 %/day	**A_s = 0.005 %/day**	**A_s = 0.006 %/day**

Top (a)	0.51	0.85	0.89
Middle (b)	0.50	0.83	0.97
Bottom (c)	0.47	0.82	0.96
Top (d)	0.37	0.0	0.0
Middle (e)	0.48	0.56	0.07
Bottom (f)	0.86	0.46	0.0
Mean	0.54	0.62	0.51

6. Conclusion

The deformation of a 500 m deep salt gallery has been monitored from April 2017 to April 2019 by repeated static lidar acquisitions. After two years, the horizontal deformation is estimated and ranges from 0.10 to 0.30% along the gallery. The detected deformation is higher than the uncertainty, which has a mean value of 0.08%. The comparisons of measurements conducted in the waste storage are consistent with our measurements. The horizontal deformation time series are then used to parametrize the mechanical behaviour law of the surrounding medium in a geomechanical model. The results confirm the values obtained in laboratory tests.

Despite the absence of a stable reference site, the acquisitions have been successfully referenced to each other. A new methodology was developed for this purpose. At least seven specific reflectors have to be used as markers and must remain at the same location for the duration of the monitoring. The methodology relies on two assumptions: point clouds acquired from a similar point and small displacement of the reflectors between the two campaigns.

Through our work, the lidar device is shown to be a useful and polyvalent tool to monitor underground cavities and to mechanically characterize the surrounding medium. In addition, the new methodology offers a new way to monitor the deformation of underground galleries, to coincide with the many existing methods.

Acknowledgement

The authors are grateful to the MDPA and DREAL for their encouraging support, their trust, and their permission to study the underground gallery. The study is financially supported by the MDPA. This work is dedicated to François H. Cornet who passed away in 2020. The authors pay homage to this scientist by acknowledging the tremendous advances in the discipline of geomechanics he accomplished over the course of his entire career.

References

Baumann, H., Illies, J.H., 1983. Stress Field and Strain Release in the Rhenish Massif, in: Fuchs, K., von Gehlen, K., Mälzer, H., Murawski, H., Semmel, A. (Eds.), Plateau Uplift. Springer Berlin Heidelberg, Berlin, Heidelberg, pp. 177–186. https://doi.org/10.1007/978-3-642-69219-2_25

Camusso, M., Billaux, D., 2013. Evaluation des flux potentiels de saumure contaminée à partir du stockage de Wittelsheim (No. 13R–001/A3). Itasca.

Carter, N.L., Horseman, S.T., Russell, J.E., Handin, J., 1993. Rheology of rocksalt. Journal of Structural Geology 15, 1257–1271. https://doi.org/10.1016/0191-8141(93)90168-A

Cecchetti, M., Rossi, M., Coppi, F., Bicci, A., Coli, N., Boldrini, N., Preston, C., 2017. A novel radar-based system for underground mine wall stability monitoring, in: Proceedings of the First International Conference on Underground Mining Technology. Presented at the First International Conference on Underground Mining Technology, Australian Centre for Geomechanics, Perth, pp. 431–443. https://doi.org/10.36487/ACG_rep/1710_34_Cecchetti

Cornet, F.H., Burlet, D., 1992. Stress field determinations in France by hydraulic tests in boreholes. J. Geophys. Res. 97, 11829. https://doi.org/10.1029/90JB02638

Delaloye, D., Diederichs, M.S., Walton, G., Hutchinson, J., 2015. Sensitivity Testing of the Newly Developed Elliptical Fitting Method for the Measurement of Convergence in Tunnels and Shafts. Rock Mechanics and Rock Engineering 48, 651–667. https://doi.org/10.1007/s00603-014-0566-0

Eitel, J.U.H., Höfle, B., Vierling, L.A., Abellán, A., Asner, G.P., Deems, J.S., Glennie, C.L., Joerg, P.C., LeWinter, A.L., Magney, T.S., Mandlburger, G., Morton, D.C., Müller, J., Vierling, K.T., 2016. Beyond 3-D: The new spectrum of lidar applications for earth and ecological sciences. Remote Sensing of Environment 186, 372–392. https://doi.org/10.1016/j.rse.2016.08.018

Errington, A.F.C., Daku, B.L.F., Prugger, A., 2010. Closure monitoring in Potash Mines using LiDAR, in: IECON 2010 - 36th Annual Conference on IEEE Industrial Electronics Society. Presented at the IECON 2010 - 36th Annual Conference of IEEE Industrial Electronics, IEEE, Glendale, AZ, USA, pp. 2823–2827. https://doi.org/10.1109/IECON.2010.5675071

Ghoreychi, M., 1991. Comportement du sel broyé sous l'effet d'une source de chaleur dans des sondages réalisés dans une mine de sel. EUR(Luxembourg).

Girardeau-Montaut, D., 2011. Cloudcompare-open source project. OpenSource Project.

Grenon, M., Caudal, P., Amoushahi, S., Turmel, D., Locat, J., 2017. Analysis of a Large Rock Slope Failure on the East Wall of the LAB Chrysotile Mine in Canada: Back Analysis, Impact of Water Infilling and Mining Activity. Rock Mech Rock Eng 50, 403–418. https://doi.org/10.1007/s00603-016-1116-8

Habib, A., 2018. Accuracy, quality, assurance and quality control of light detection and ranging mapping, in: Topographic Laser Ranging and Scanning: Principles and Processing. Taylor & Francis, Boca Raton, pp. 291-313. https://doi.org/10.1201/9781315154381.

Han, J.-Y., Guo, J., Jiang, Y.-S., 2013. Monitoring tunnel profile by means of multi-epoch dispersed 3-D LiDAR point clouds. Tunnelling and Underground Space Technology 33, 186–192. https://doi.org/10.1016/j.tust.2012.08.008

Itasca, 2002. Flac3D User's Guide.
JCGM, 2008. Evaluation of measurement data — Guide to the expression of uncertainty in measurement (No. 100:2008). Joint Committee for Guides in Metrology.
Kazhdan, M., Bolitho, M., Hoppe, H., 2006. Poisson Surface Reconstruction. Symposium on Geometry Processing 10 pages. https://doi.org/10.2312/SGP/SGP06/061-070
Khaledi, K., Mahmoudi, E., Datcheva, M., Schanz, T., 2016. Stability and serviceability of underground energy storage caverns in rock salt subjected to mechanical cyclic loading. International Journal of Rock Mechanics and Mining Sciences 86, 115–131. https://doi.org/10.1016/j.ijrmms.2016.04.010
Kukutsch, R., Kajzar, V., Konicek, P., Waclawik, P., Ptacek, J., 2015. Possibility of convergence measurement of gates in coal mining using terrestrial 3D laser scanner. Journal of Sustainable Mining 14, 30–37. https://doi.org/10.1016/j.jsm.2015.08.005
Laouafa, F., Pinte, J., Ghoreychi, M., 2010. Etude géomécanique du stockage de StocaMine (No. DRS10 – 108130– 14273A). INERIS.
Larroque, J.-M., 1987. Analyse de la déformation de la série salifère du bassin potassique de Mulhouse, et évolution du champ de contraintes dans le sud du fossé rhénan au tertiaire et à l'actuel. PhD thesis. Montpellier, France.
Lichti, D.D., Licht, M.G., 2006. Experiences with terrestrial laser scanner modelling and accuracy assessment. Int. Arch. Photogramm. Remote Sens. Spat. Inf. Sci 36, 155–160.
Lynch, B.K., Marr, J., Marshall, J.A., Greenspan, M., 2017. Mobile LiDAR-Based Convergence Detection in Underground Tunnel Environments.
Modeste, G., 2020. Estimation et évolution des vides miniers aux Mines Domaniales de Potasse d'Alsace (MDPA) par mesures géodésiques et modélisation géomécanique. PhD thesis, University of Strasbourg, France.
Nguyen-Minh, D., Bergues, J., 1995. A global approach to the short term response of a hard marl, in: 8th ISRM Congress. Presented at the 8th ISRM Congress, International Society for Rock Mechanics and Rock Engineering, Tokyo, Japan, pp. 303–306.
Pejić, M., 2013. Design and optimisation of laser scanning for tunnels geometry inspection. Tunnelling and Underground Space Technology 37, 199–206. https://doi.org/10.1016/j.tust.2013.04.004
Petrie, G., Toth, C.K., 2018. Terrestrial laser scanners, in: Topographic Laser Ranging and Scanning: Principles and Processing. Taylor & Francis, Boca Raton, pp. 29-88. https://doi.org/10.1201/9781315154381.
Tarantola, A., 2005. Inverse Problem Theory and Methods for Model Parameter Estimation. Society for Industrial and Applied Mathematics. https://doi.org/10.1137/1.9780898717921
Telling, J., Lyda, A., Hartzell, P., Glennie, C., 2017. Review of Earth science research using terrestrial laser scanning. Earth-Science Reviews 169, 35–68. https://doi.org/10.1016/j.earscirev.2017.04.007
Trippetta, F., Collettini, C., Meredith, P.G., Vinciguerra, S., 2013. Evolution of the elastic moduli of seismogenic Triassic Evaporites subjected to cyclic stressing. Tectonophysics 592, 67–79. https://doi.org/10.1016/j.tecto.2013.02.011
Walton, G., Diederichs, M.S., Weinhardt, K., Delaloye, D., Lato, M.J., Punkkinen, A., 2018. Change detection in drill and blast tunnels from point cloud data. International Journal of Rock Mechanics and Mining Sciences 105, 172–181. https://doi.org/10.1016/j.ijrmms.2018.03.004
Wang, T., Yan, X., Yang, X., Yang, H., 2010. Dynamic subsidence prediction of ground surface above salt cavern gas storage considering the creep of rock salt. Sci. China Technol. Sci. 53, 3197–3202. https://doi.org/10.1007/s11431-010-4172-4
Wang, W., Zhao, W., Huang, L., Vimarlund, V., Wang, Z., 2014. Applications of terrestrial laser scanning for tunnels: a review. Journal of Traffic and Transportation Engineering (English Edition) 1, 325–337. https://doi.org/10.1016/S2095-7564(15)30279-8